On the Correlation between the SAR Backscatter Modulation and Surface Waves Orbital Velocity

N.B. When citing this work, cite the original published paper.

(article starts on next page)

On the Correlation Between the SAR Backscatter Modulation and Surface Waves Orbital Velocity

Anis Elyouncha , *Member, IEEE*, and Roland Romeiser , *Senior Member, IEEE*

Abstract—**A challenging effect in the retrieval of ocean surface currents from synthetic aperture radar (SAR) is the so-called wave-induced Doppler velocity. This effect arises from the correlation between the modulation of the normalized radar cross section (NRCS) caused by the slopes of the long waves and the modulation of the Doppler shift resulting from their orbital velocities. In this article, we analyzed six acquisitions of high-resolution interferometric SAR images of collocated NRCS and Doppler frequency shift acquired by the along-track interferometric SAR TanDEM-X at two polarizations VV and HH. The unique high-quality wave-resolving interferograms of TanDEM-X allow a detailed investigation of the wave-induced Doppler at scales rarely available from space. These images are acquired in different regions, times, and satellite passes (ascending or descending), thus capture different wave conditions in height and propagation direction. First, it is shown that in cases of range propagating waves, the NRCS and Doppler shift modulations are highly correlated. The sign of the correlation coefficient depends on the direction of propagation of the wave relative to the SAR. Moreover, it is shown that the NRCS-Doppler correlation affects the mean Doppler shift and that the wave-induced Doppler velocity increases with the wave steepness. In cases of azimuth propagating waves, the linear correlation is very low due to large phase difference between the NRCS and the Doppler shift modulations. Consequently, the wave-induced Doppler velocity is negligible. Finally, the wave-induced Doppler, if not taken into account, can bias the ocean current estimation by up to 0.96 m/s.**

Index Terms—**Along-track interferometry (ATI), ocean surface currents and waves, synthetic aperture radar (SAR) Doppler centroid (Dc), TanDEM-X.**

I. INTRODUCTION

OCEAN surface currents can be measured using different sensors and techniques. This article focuses on the wave contribution to current measurements using microwave Doppler radars, which includes synthetic aperture radar (SAR) and Doppler scatterometers. This is investigated for the first time using data obtained from a spaceborne SAR.

Anis Elyouncha is with the Department of Marine Sciences, University of Gothenburg, 413 90 Gothenburg, Sweden, and also with Department of Space, Earth and Environment, Chalmers University of Technology, 412 96 Gothenburg, Sweden (e-mail: anis.elyouncha@gu.se).

Roland Romeiser is with the Rosenstiel School of Marine and Atmospheric Science, University of Miami, Coral Gables, FL 33146 USA (e-mail: rromeiser@miami.edu).

It has been known since the early theoretical [1] and experimental [2] work on microwave Doppler spectra by D. R. Thompson and the numerical study by Romeiser and Thompson [3] that the phase velocity of the two Bragg wave components, the different modulations of the two Bragg wave components by the orbital motions of longer waves, and the correlation between variations of the effective line-of-sight (radial) velocities of the scatterers and the local normalized radar cross section (NRCS) along the longer waves contribute significantly to the observed Doppler frequencies. Since the mean Doppler frequency shift (Doppler centroid, Dc) is the NRCS-weighted average of the Doppler frequencies in the resolution cell, the NRCS-Dc correlation induces a net velocity even in the absence of currents.

There are two major methods for deriving ocean surface velocity from SAR data [4]: Along-track interferometry (ATI) and the Doppler centroid anomaly analysis (DCA). The retrieval of surface velocity from ATI-SAR data has been demonstrated in several papers, e.g., [5], [6], and [7]. It has been shown that ATI-SAR is capable of providing high spatial resolution ($\sim$100 m) surface velocity maps, very close to the coastline, with a high accuracy. The DCA method was first introduced in [8] and further demonstrated from satellite observations using the C-band ENVISAT/ASAR data in [9] and [10]. The DCA method generates surface velocity at a spatial resolution of $\sim$ 1–2 km. Results of retrieving surface currents using the DCA method from ENVISAT/ASAR and Sentinel-1 data have been reported in several works, e.g., [11], [12], [13], and [14].

The wave contribution to the SAR-observed Doppler shift, commonly referred to as wave-induced Doppler shift, wave Doppler bias, or wind-wave-induced artifact surface velocity [15], has been more recently demonstrated by relating the SAR-observed Dc to wind vectors and/or wave parameters using the C-band Sentinel-1 data [16] and the X-band TanDEM-X data in [17]. It has now been recognized that in order to retrieve accurate ocean surface currents from SAR Doppler shift, the wave-induced Doppler shift must be accurately estimated and removed [7], [13], [15]. This makes deriving surface currents from SAR challenging.

The wave Doppler bias is an important issue for ATI, DCA, and Doppler Scatterometry [18]. A few theoretical models have been proposed [1], [3], [8], [9] to predict the mean Doppler shift from the wave height spectrum and a modulation transfer function (MTF). Other empirical or semiempirical models [16], [17], [18], [19] based on matching the observed Dc with the radial wind speed and/or wave parameters or based on empirical MTFs [20], [21], [22]. The wind is usually used as a proxy to the

wave slopes. These models can explain the mean effect of the contributions of the Bragg wave motions and longer wave orbital motions to the Dc relatively well. Yet, high quality images of the longer waves observed from space that resolve the variations of the Doppler along these waves, have not been available to study the wave Doppler bias at small scales. This study addresses this gap in knowledge. Here, we present the first analysis of very high resolution interferograms from the spaceborne ATI-SAR system TanDEM-X that resolve spatial Doppler variations together with the corresponding NRCS variations on scales down to tens of meters. This TanDEM-X dataset offers a unique opportunity to study the relationship between NRCS and Doppler variations along surface waves in detail due to the good quality of the TanDEM-X interferograms, which resolves the spatial variations of both quantities. This has not been possible with ATI-SAR systems such as SRTM [23] and TerraSAR-X [6] in divided-antenna mode, and conventional single SAR, e.g., Sentinel-1 [13] and Doppler scatterometry [18], because the interferometric time lags of these systems are shorter than the two-satellite ATI-SAR system . Thus, to achieve the same precision as TanDEM-X, a larger number of looks have to be averaged resulting in a coarse resolution Doppler grids.

In this study, we investigate the correlation between the NRCS and the Dc variations, which is responsible for wave-induced Doppler velocity, through analysis of six case studies observed by the ATI-SAR TanDEM-X. While previous research has shown this correlation in the temporal domain using a sea platform-based scatterometer [24], it lacked further quantitative investigation. In the spatial domain (SAR image domain), the wave pattern in TanDEM-X images has been shown by Romeiser et al. [6], albeit without a detailed examination of the relationship between NRCS and Dc variations. This article contributes a more detailed analysis of this relationship, alongside an evaluation of its impact on mean Doppler shift estimation at both VV and HH polarizations.

II. BACKGROUND AND METHODS

A. Background

SAR measures the NRCS (also called backscatter) and the Doppler frequency shift, also called Dc. The NRCS responds mainly to the surface roughness, thus, over sea, it is used to retrieve wind speed and wave height. The Doppler shift responds to the surface motion, thus can be used to infer the surface velocity. A single-beam SAR is only capable of measuring the radial component of the surface velocity (RVL, also called Doppler velocity U_D). Typically, a spaceborne SAR carries a right looking antenna with line-of-sight perpendicular to the flight direction.

The Dc can be virtually decomposed into different components attributed to different sources of motion

$$f_{\text{Dc}} = f_{\text{geom}} + f_{\text{phys}} + f_{\text{error}} \tag{1}$$

where f_{geom} is due to satellite velocity relative to solid rotating Earth, antenna electronic mispointing and the scalloping effect in the azimuth direction (in case of ScanSAR imaging mode). This requires accurate orbital/attitude parameters to be estimated [16]. f_{phys} is due to ocean surface currents and waves.

f_{error} groups all sources of errors. Usually Doppler calibration is needed to estimate f_{error}, which requires a reference (in height and velocity). In this work, the land is used as a reference (zero velocity) to calibrate the observed Dc.

The physical (after removing the geometrical Doppler shift due to the satellite motion) Doppler shift observed by SAR can be expressed as [3], [8], [9]

$$f_{\text{phys}} = -\frac{k_e \sin \theta}{\pi} U_D \tag{2}$$

where k_e is the electromagnetic wavenumber and θ is the incidence angle.

To get an idea how challenging it is to get accurate surface currents from SAR, the variation of f_{phys} in (2) can be expressed as a function of the variation of U_D, i.e., $\Delta f_{\text{phys}} = (-k_e \sin \theta / \pi) \Delta U_D$. For instance, if a precision of $\Delta U_D = 0.1$ m/s is required, it implies a Doppler precision of $\Delta f_{\text{phys}} = 3.7$ Hz, (X-band) at $\theta = 35°$.

SAR observes the ocean velocity integrated over its resolution cell (few meters) and temporally over its integration time (~ 1 s). The radial sea surface velocity, i.e., the surface velocity projected on the radar ground range, U_D, can be decomposed into three components as follows [9]:

$$U_D = U_c + C_{\text{BW}} + C_{\text{LW}}. \tag{3}$$

The first term is the surface current velocity projected on the ground range, i.e., $U_c = |U_c| \cos \varphi_c$, where $|U_c|$ is the surface current magnitude and φ_c is its angle relative to the line-of-sight. This term is independent of frequency and polarization but depends on the azimuth angle of the radar. The second term is due to the Bragg waves phase speed, which depends on the frequency, incidence angle, and azimuth angle. For instance, at an incidence angle of 30°, the Bragg wave phase speed is 31 cm/s for X-band. The last term is due to the orbital velocities of the long waves (at least three times longer than the Bragg waves). This term is dependent on frequency, polarization, incidence angle, and azimuth angle. The dependence of C_{BW} and C_{LW} on the azimuth angle is implicit. The full formulas of these two terms can be found in several references, e.g., [17], [20], and [25]. The dependence on polarization is due to the fact that the orbital velocities are weighted by the backscatter, which depends on polarization. The orbital velocities contribution can be up to 1 m/s [8], [15], [17], [20]; hence it is expected to be the dominant term in most cases. C_{LW} can be expressed as [3], [8], [9]

$$C_{\text{LW}} = \frac{\langle \sigma' f_D' \rangle}{\langle \sigma \rangle} \tag{4}$$

where σ' and f_D' are the (zero mean) variations of the NRCS and the Doppler shift, respectively. $\langle \sigma \rangle$ is the mean NRCS.

Two cases must be distinguished. Subresolution waves, i.e., the wavelength of the modulating wave is smaller than the radar resolution cell, wave-induced Doppler velocity is the backscatter-weighted average of the orbital velocities inside the resolution cell. In the second case, the wavelength of the modulating wave is larger than twice the radar resolution cell, i.e., the wave is phase-resolved. In this latter case, the orbital velocity adds as a local current.

B. ATI Technique

First, the interferogram is formed from two single-look complex (SLC) coregistered images acquired within a small time lag, also called temporal baseline. The interferometric phase is usually estimated by averaging the complex interferogram [26]

$$\phi = \arg\left\{\sum s_1 s_2^*\right\} = \arg\left\{\sum |s_1||s_2|\exp j(\phi_1 - \phi_2)\right\} \tag{5}$$

where s_1 and s_2 are the two interfered complex images, $|s_1|$ and $|s_2|$ denote their magnitudes, ϕ_1 and ϕ_2 denote their phases, and $*$ denotes the complex conjugate. The sea surface is dynamic, hence the time delay between acquisitions suitable for interferometry is limited by the decorrelation time of the velocity field to a few milliseconds. The summation is usually performed over a certain area around the pixel, where the phase is assumed to be homogeneous. The estimated phase is the power-weighted mean of the surrounding phases. That is if the interferogram is averaged over an area of varying NRCS, e.g., due to a modulating wave, the mean phase will be biased toward the phase (velocity) of the strong scatterers.

Some ATI systems such as TanDEM-X are not a pure along-track interferometric system, but a hybrid (across- and along-track) interferometric SAR. Thus, the observed phase is sensitive to both topography and displacement. Assuming the baseline and surface displacement are small compared to the range, the observed phase can be decomposed as [27]

$$\phi_{\text{observed}} = \phi_{\text{topo}} + \phi_{\text{disp}} + \phi_{\text{atmos}} + \phi_{\text{error}} + 2n\pi \tag{6}$$

where ϕ_{topo} is the topographic phase, ϕ_{disp} is the displacement phase, ϕ_{atmos} is the phase due to atmospheric delay, n is an integer, and ϕ_{error} groups all type of systematic errors (bias) and random errors (noise).

All contributions other than the displacement (ϕ_{disp}) must be removed. The atmospheric phase is negligible given the very small time delays, between the two SLCs, considered here ($\lesssim$ 5 ms). The topographic phase is removed using a geoid and a digital elevation model (DEM). Here, the EGM2008[1] and the Copernicus DEM called COP-DEM_GLO-90[2] are used. At this stage, the interferometric phase is ambiguous and only known within 2π. In order to be able to relate the interferometric phase to velocity, the phase must first be unwrapped. The topographic phase removal and phase unwrapping is done using the GAMMA software [28]. Once the interferogram is unwrapped, the Dc and velocity values can be derived.

The Dc is derived from the estimated interferometric phase ϕ as

$$\text{Dc}_{\text{ATI}} = \frac{1}{2\pi\tau}\phi_{\text{disp}} \tag{7}$$

where τ is the interferometric time lag between the two SLCs, which is typically about few milliseconds.

[1][Online]. Available: https://earth-info.nga.mil/
[2][Online]. Available: https://spacedata.copernicus.eu/web/cscda/dataset-details?articleId=394198

C. DCA Technique

There are two techniques for estimating the Dc from a single-antenna Doppler radar [29]: time-domain estimation based on the phase- and frequency-domain estimation based on the Doppler spectrum. The first method is the most commonly used because of its simplicity and computational efficiency. Moreover, it is applicable to both conventional single-antenna SAR and Doppler scatterometer, while the second method is only applicable to SAR. Thus, the second method is not discussed here. The first method, also called pulse-pair method or average cross-correlation coefficient, calculates the complex correlation to estimate Dc, and subsequently, the velocity along the line of sight (RVL).

The complex correlation coefficient of two samples z separated by k is given by

$$\rho(k) = \frac{1}{N-1}\sum_{n=0}^{N-1} z(n+k)z^*(n) \tag{8}$$

where N is the number of pulses used to form the interferogram. The phase of the correlation function is directly related to the Dc.

The estimate of Dc is given by

$$\text{Dc}_{pp} = \frac{1}{2\pi k T_p}\phi_{pp} \tag{9}$$

where $\phi_{pp}(= \arg\{\rho(k)\})$ is the phase of the correlation coefficient, i.e., phase difference between consecutive pulses, k is usually set to 1, and T_p is the pulse repetition interval (PRI), which typically varies between 0.3 and 1 ms.

D. Simulation of NRCS and Dc Modulations

In this section, the variation of the NRCS by a long modulating wave and the variation of the Dc due to the orbital velocities of the long wave is simulated. The simulation is based on a monochromatic 1-D wave propagating in the range direction or azimuth (flight) direction. The effect of the correlation between the NRCS and Dc variations on the mean Doppler shift, i.e., Dc, is also calculated.

Fig. 1 (upper panel) depicts the satellite acquisition geometry used for the simulation. A satellite at an altitude (500 km) similar to the nominal altitude of TanDEM-X, illuminating the sea surface with incidence angles varying between 20° and 40°. Fig. 1(b) and (c) depicts the surface elevation (η), the radial wave orbital velocity (u_r), and the NRCS modulation (σ'/σ), for a range traveling wave (b) and azimuth traveling wave (c). Here, we have used a simple linear MTF to calculate the modulation in the backscatter due to the slopes of the wave [30], [31]. The orbital velocities are calculated analytically and projected on the line of sight of the SAR (see Appendix A for details).

For the range traveling wave [see Fig. 1(b)], the NRCS and the Dc modulations peak at very close positions over the wave profile, hence the small phase difference between the two modulations. This is because the tilt part of the MTF, which usually dominates, peaks at the zero crossing of η where the slope is maximum. The hydrodynamic MTF peaks somewhere
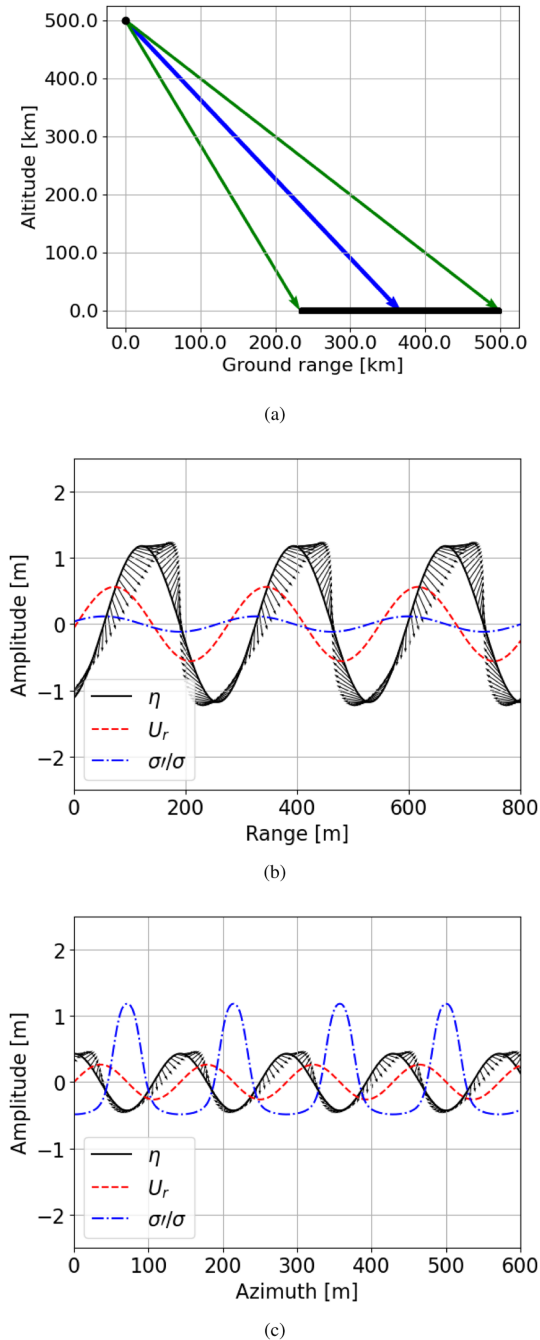
(a)

(b)

(c)

Fig. 1. (a) Satellite geometry. (b) Range traveling wave (a=1.18 m and λ=272 m). (c) Azimuth traveling wave (a=0.43 m and λ=143 m). η: Wave amplitude, U_r: Radial velocity, and σ'/σ: NRCS Modulation. The wave is propagating from left to right. The arrows depict the wave orbital velocities.

between the zero crossing and maximum of eta, depending on the relaxation rate. The radial velocity also peaks somewhere between the zero crossing and the maxima of η depending on the incidence angle. Note that the velocity bunching MTF vanishes in the range direction (see Appendix A).

For the azimuth traveling wave, only the vertical component of the orbital velocity has nonzero projection on the SAR line of sight. Thus, the Dc will always peak at the same position

over the wave profile, i.e., at the zero crossing of η, and it will reverse sign depending on the wave propagation direction. The NRCS modulation will peak at the maxima or minima of η depending on the wave propagation direction. Thus, the phase difference between the NRCS modulation and the Dc modulation will be $\sim 90°$, as it can be observed in Fig. 1(c). Note that this analysis assumes a linear NRCS modulation or weakly non-linear such as the case presented here. In nonlinear cases, the NRCS modulation is strongly distorted and this $\sim 90°$ phase difference does not hold.

The NRCS-weighted average of the Doppler shift is calculated using (4). The calculation was done for the significant wave height (SWH) (2.36, 1.5, 2.3, 5.5 m), wavelengths (272.2 m, 228.8, 279.3, 208.1 m), and incidence angles (35, 35, 30, 30) corresponding to the four near-range traveling wave fields observed by SAR (see Tables I–III) and analyzed later. The calculation of the NRCS-weighted mean Dc yields 3.47, 1.81, 3.25, and 28.33 Hz, for the four range traveling cases. When converted to radial velocity, using the TanDEM-X frequency (9.65 GHz), this translates into 0.052, 0.027, 0.049, and 0.42 m/s. Note that, for simplicity, we have omitted the integration over the SAR integration time, which would give an even higher mean Dc. For the azimuth traveling wave, the NRCS-weighted average of the Doppler shift vanishes, i.e., theoretically zero, because the NRCS modulation maxima coincide with the zero radial velocity.

This simple simulation shows that the NRCS-weighted average of the Doppler shift yields a net Doppler shift even when the mean orbital velocity is zero (according to the linear wave theory) and even in the absence of current. Thus, SAR will always measure a net Doppler shift, and thus, a net velocity except in case of pure azimuth traveling waves. This emulates, in an idealized way, the SAR imaging inside the resolution cell. This also emulates spatial averaging of the complex interferometric phase in the presence of long resolved waves, e.g., swell.

III. DATASETS

A. TanDEM-X Data

TanDEM-X is a system of two satellites flying in tandem and carrying almost identical X-band SAR sensors [32]. The images used here are part of the coregistered single look complex (CoSSC) dataset. These images are acquired with the stripmap bistatic mode. The scene size of each acquisition is approximately 50 km in azimuth and 30 km in range. The raw resolution of the SLC data is $\sim$1.5 and $\sim$2.5 m in ground range and azimuth, respectively. The center frequency of TanDEM-X SAR is 9.65 GHz. The main acquisition parameters of the images studied here are given in Table I. The area covered by the satellite acquisition is shown in Fig. 2.

The NRCS is calculated as follows:

$$\sigma^0 = K|\text{DN}|^2 \sin\theta - \text{NESZ} \qquad (10)$$

where K is the calibration factor provided in the TanDEM-X product, DN is the digital number (amplitude of the SAR image), and NESZ is the noise equivalent sigma zero. Since, we are

TABLE I
TanDEM-X Acquisition Parameters

Date Time	$\langle\theta\rangle$	Heading [deg]	τ [deg]	polarization [s]	Pixel size [m]	N-looks Rg/Az [m]	Image size Rg/Az[km]
2014-09-02 06:36:01	34.82	190.49	6.52e-04	VV / HH	1.56 / 2.56	25	7.8 / 12.8
2014-09-13 06:35:39	34.78	190.57	0.0019	VV / HH	1.56 / 2.56	25	11.7 / 13.2
2015-10-12 02:00:59	31.30	349.46	0.0047	VV	1.76 / 2.08	25	8.8 / 10.4
2016-01-04 06:41:45	31.08	192.18	0.0043	VV	1.76 / 2.08	25	8.8 / 10.4
2014-09-14 14:16:18	21.28	191.23	0.0062	VV / HH	2.50 / 2.40	10	9.6 / 10
2020-06-07 17:47:01	34.35	348.15	0.0059	VV	1.70 / 1.90	10	8.5 / 9.5

θ is the incidence angle and τ is the interferometric time lag. The pixel size is for the single look, N-looks is the number of averaged looks, and image size is the size of the images shown in Figs. 4–9.

TABLE II
In Situ Wave Parameters

Buoy ID	LAT [deg]	LON [deg]	Date	$VHM0$ [m]	$VTPK$ [s]	λ_{VTPK} [m]	$VTZA$ [s]	λ_{VTZA} [m]	VPED [deg]	VMDR [deg]	WDIR [deg]
6200069	48.29	-4.9683	2014-09-02T06:36	2.36	12.9	313.3			275.26		
6200103	49.9	-2.90	2014-09-13T06:30	0.70			6.0	56.21			60.0
46026	37.75	-122.82	2015-10-12T02:00	2.32	11.9	221.1				254	
6200046	57.96	-3.33	2016-01-04T06:41	5.51	13.3	276.2	8.05	101.26	93.2		
46215	35.2	-120.86	2014-09-14T14:16	0.86	11.1	192.7				234	
46011	35.0	-120.99	2014-09-14T14:16	1.01	9.1	129.3				295	313

VHM0 is the spectral SWH, VTPK is wave period at spectral peak / peak period (Tp), VTZA is the average zero crossing wave period (Tz), VPED is the wave principal direction at spectral peak, and VMDR is mean wave direction from. λ_{VTPK} and λ_{VTZA} are the peak and zero-crossing wavelength calculated from VTPK and VTZA, respectively, using the dispersion relation. WDIR is the wind direction from.

interested only in the zero-mean variation, both the NRCS and Doppler shift are detrended in range and azimuth.

As mentioned before, the radar measures the power-weighted mean radial velocity. The average is taken over the scatterers in the resolution cell and integration time. Here, the NRCS-weighted mean of the Doppler shift is calculated over a portion of the image. This does not reproduce exactly the subresolution imaging process, but it illustrates well the NRCS-Doppler correlation-induced bias.

To reduce the phase noise and increase the phase precision, the interferogram is multilooked, which downgrades the spatial resolution. The single-look pixel size and the number of averaged pixels (N-looks) for each image are reported in Table I. Finally, it was found that the Dc estimated from TanDEM-X is biased, i.e., nonzero over land, and varies with elevation angle (range). The estimated Dc is calibrated using land as a reference. The bias estimated over land is applied to the Dc over sea.

B. In Situ Data

Wave buoy data were available online[3] for five satellite acquisitions. For the sixth acquisition, no buoy was found in the surrounding area. Table II summarizes the relevant wave parameters as measured by these buoys interpolated at the satellite acquisition time. Note that these buoys do not always provide all the wave parameters for all satellite acquisitions, hence the missing data in Table II. Note also that buoys provide sometimes different quantities, e.g., mean and peak. Finally, most of the wave buoys are located outside the satellite image except the

third and fifth acquisitions where it is located on the western edge of the image. Particularly in the second acquisition, the buoy is located far from the image. The locations of the used buoys are depicted in Fig. 2.

C. Model Data

Since the analyzed images do not always coincide with wave buoys and these buoys when available do not always measure all wave parameters, model data are also used to support the analysis. The wind and wave parameters are extracted from the European Centre for Medium Range Weather Forecasts (ECMWF) reanalysis product ERA5. ERA5 provides hourly estimates on a 31-km grid.[4] The most relevant parameters to this study are shown in Table III. For instance, based on model data in Table III for the first acquisition, two wave systems propagating roughly in opposite direction are present in the area. A wind wave with a SWH of 0.42 m is coming from 60° and a swell with SWH= 2.38 m is coming from 292°. This corresponds to a swell moving toward the SAR roughly in the range direction.

IV. Results

A. Effect of Averaging on the Mean Doppler Shift

As mentioned previously, the NRCS and Doppler images were detrended in range and azimuth to remove low-frequency variations, which might be due to spatial variation of the wind and current for instance. After detrending, a nonweighted mean of the variations of the NRCS and Doppler shift is zero.

[3][Online]. Available: https://marineinsitu.eu/

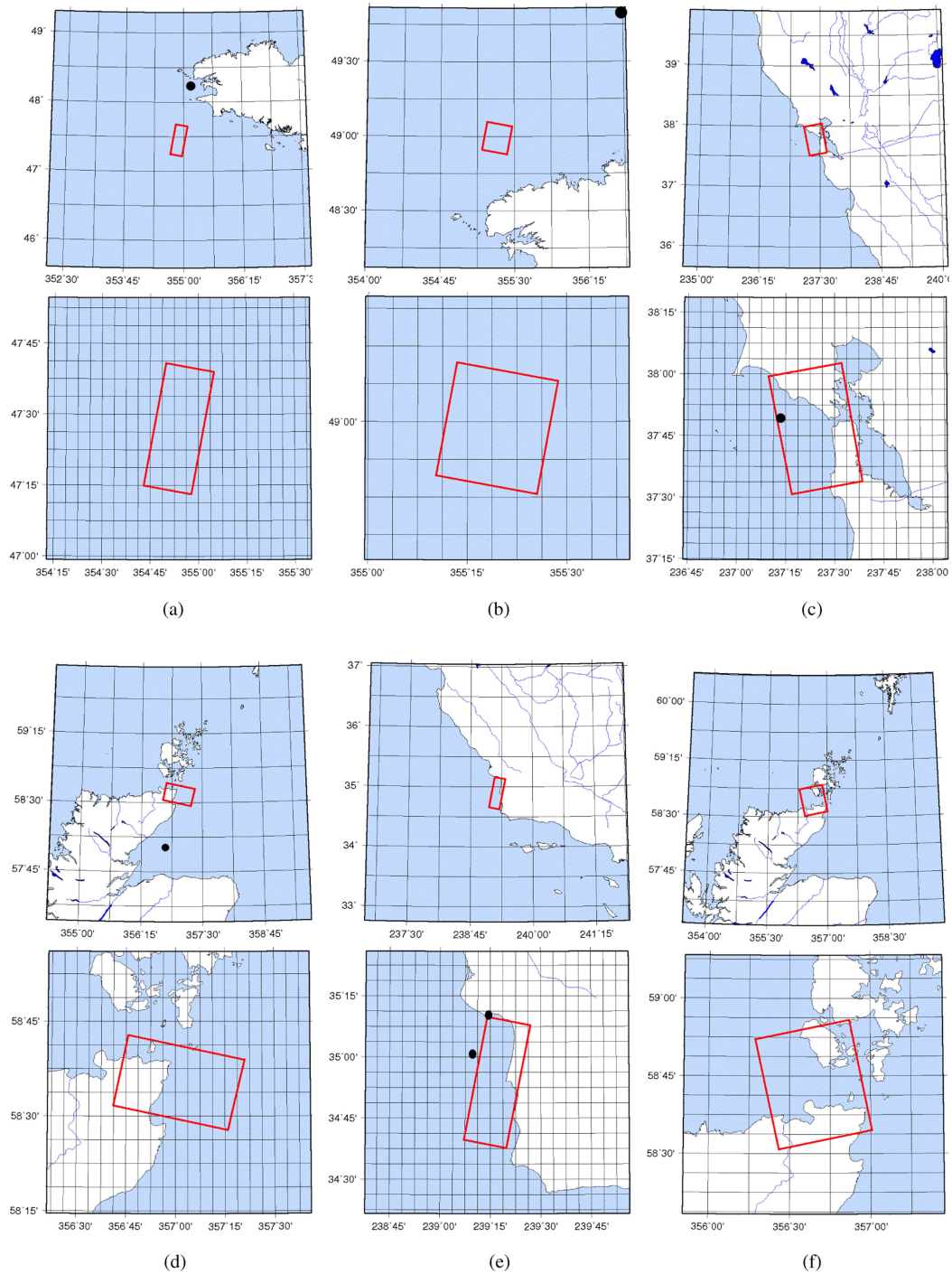[4][Online]. Available: https://confluence.ecmwf.int/display/CKB/ERA5

Fig. 2. Geographical locations of the selected data. (a) Iroise Sea 2014-09-02. (b) English Channel 2014-09-13. (c) S. Francisco Bay 2015-10-12. (d) Moray Firth 2016-01-04. (e) Santa Maria 2014-09-14. (f) Pentland Firth 2020-06-07. The lower panels are zoomed in views of the upper panels. The red frames represent the swaths of TanDEM-X. The black dots show the locations of the wave buoys when they are available.

The purpose of this section is to investigate the dependence of the mean Dc on the spatial resolution or the spatial extent of the averaging (multilooking) area. The ATI-SAR interferogram is a complex image, thus averaging the interferogram, and then, taking the phase of the averaged interferogram is equivalent to calculating the NRCS-weighted average of the ATI-SAR phase, from which the radial velocity is estimated. The question is whether the averaging process affects the mean phase, and hence, mean radial velocity?

In order to investigate this effect, the complex interferogram has been processed with different averaging areas ranging from 10 to 400 m. For simplicity, this has been done only for the

TABLE III
WIND AND WAVES PARAMETERS

Date Time	WS [m/s]	WD [deg]	$mdww$ [deg]	$mdts$ [deg]	$shww$ [m]	$shts$ [m]	T_p [s]	λ_p [m]	T_{m02} [s]
2014-09-02 06:36:01	5.77	62.3	59.7	292.1	0.4	2.3	13.2	272.2	
2014-09-13 06:35:39	6.19	82.6	82.9	260.37	0.41	1.49	11.94	222.83	
2015-10-12 02:00:59	3.82	299.4	290.98	272.96	0.26	2.27	13.37	279.31	
2016-01-04 06:41:45	15.35	108.4	107.42	86.27	4.82	1.80	11.54	208.09	
2014-09-14 14:16:18	6.93	323.8	307.5	182	0.95	0.49	9.57	142.9	4.25
2020-06-07 17:47:01	7.41	353.3	348.8	346.2	1.18	2.14	9.54	142.1	4.42

WS is wind speed At 10-m height, WD is wind direction, mdww is mean direction of wind waves, mdts is mean direction of total swell, shww is significant height of wind waves, shts is significant height of total swell, T_p is peak period, and λ_p is peak wavelength. The convention for direction is coming from wrt north.
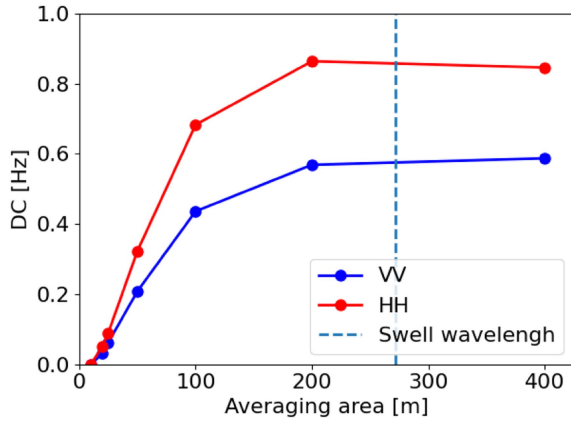

Fig. 3. Averaging effect on Dc. The mean Dc against the averaging area. For VV and HH polarizations for the first case study (2014-09-02).

first case study. The result is depicted in Fig. 3 for VV and HH polarizations, where each point is the mean Dc of the image. Note that the depicted value is relative to the smallest averaging area (10 m). First, it can be observed that the HH Dc is higher than the VV Dc in agreement with theory and previous studies, e.g., [17] and[25]. This is mainly due to the tilt MTF been higher at HH than at VV [30]. Second, it can be noticed that the Dc increases with averaging area (Number of looks) because longer waves are included in the averaging area until the longest wave has been averaged (saturation). It increases rapidly in the beginning because the shorter wind waves ($\lambda \sim 10$–100 m) are steep (larger NRCS modulation), while longer waves such as swell ($\lambda \gtrsim 100$ m) are shallower (low NRCS modulation). Note that in the monochromatic wave case, the Dc is independent of resolution or averaging area. For a random sea however, the longer resolved waves become unresolved as the averaging area increases. Note also that if the phase average is taken instead of complex average (as done here for Fig. 3), the Dc will not increase with increasing area. Nevertheless, the total increase is small, less than 1 Hz, yielding a maximum surface velocity bias of 0.027 m/s. Thus, the mean Dc can be considered as independent of resolution, unless the required accuracy is really high ($\lesssim 0.03$ m/s), then this averaging effect should be taken into account.

B. NRCS-Doppler Shift Correlation

In this section, the result of each case study is discussed separately in the following subsections. The images are presented in the SAR geometry, i.e., azimuth (flight direction) and range (antenna look direction or line of sight). For the interpretation of the following results, one should refer to Tables II and III for the wave propagation direction, and Table I for the satellite flight direction. Note that the satellite can be ascending or descending but the SAR antenna is always looking to the right of the flight direction. The NRCS and Dc variations are standardized ($(\sigma' - \langle \sigma' \rangle)/\langle \sigma'^2 \rangle)$ and $((Dc' - \langle Dc' \rangle)/\langle Dc'^2 \rangle)$ for the cross spectra and scatterplots presented as follows.

The correlation between the NRCS and the Dc is the reason why the third term of (3) does not vanish. Note, however, that the NRCS and Doppler variations shown in this section are due to resolved long waves (typically swell). This would add a bias to the Doppler shift due to unresolved waves (mostly wind-waves) within the resolution cell and the underlying current. The zero mean resolved variations vanish if the Doppler shift is averaged without weighting over an area larger than several swell wavelengths.

1) Case Study 1 (Iroise Sea): Fig. 4 depicts the 2-D zero-mean NRCS and Dc variations in (a) and (b), respectively. These images were acquired over the Iroise Sea on 2 September 2014. The images are shown only for VV polarization, as the HH polarization images look very similar. The sea state consists of a wind sea propagating from 60° (according to the model) and a swell propagating from 260° (model) and 275°(buoy). The significant wave height of the swell is larger than wind sea, i.e., swell dominant sea.

The two images (a) and (b) exhibit alternating bright/dark and positive/negative stripes in the NRCS and Dc, respectively. These Doppler stripes are clear indicator of a long wave's orbital velocities moving toward and away from the radar. Similarly, the bright and dark stripes in the NRCS are a result of tilt, range bunching, and hydrodynamic MTF due to the long wave slope and orbital velocity. That is, the NRCS is higher than the mean over the slopes tilted toward the SAR and lower than the mean over the slopes tilted away from the SAR.

The real and imaginary parts of the cross spectrum ($\mathcal{F}\{\sigma\prime\} \cdot \mathcal{F}\{Dc\prime\}^*$), where $\mathcal{F}$ is the Fourier transform, are depicted in Fig. 4(c) and (d). The swell is propagating from the west (from
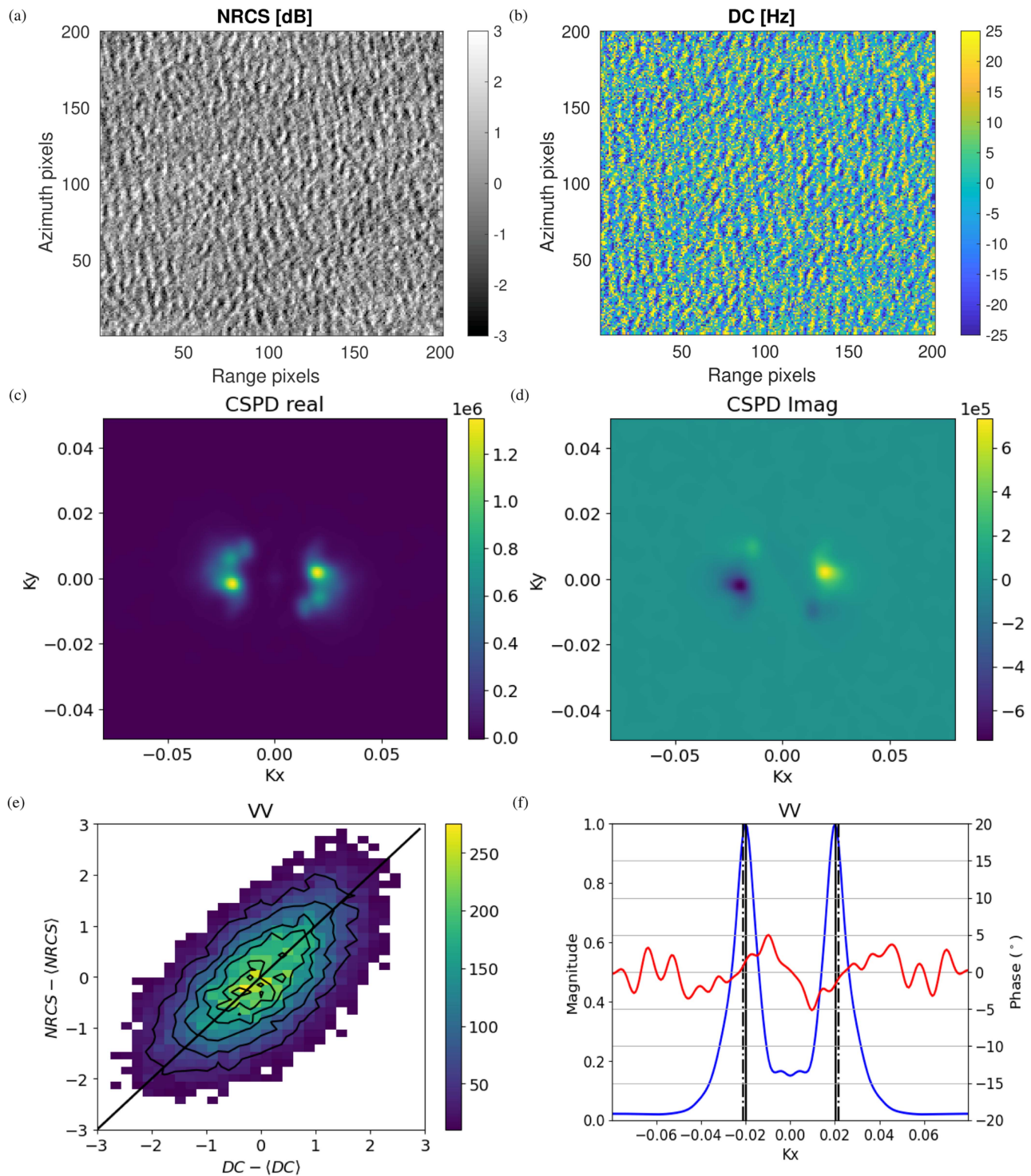
Fig. 4. Iroise Sea—2014-09-02—Descending pass. (a) NRCS variation. (b) Dc variation. (c) Real part. (d) Imaginary part of the cross spectrum. (e) Scatter plot of NRCS variation against Dc variation for VV, colorbar is the number of points. (f) Cross-spectrum magnitude normalized (blue) and phase (red) for VV, averaged over azimuth direction, K_x is the range wavenumber. The solid and dashed lines depict the wavenumber at the cross-spectrum peak and the swell given by the ocean model and the wave buoy averaged.

the Atlantic Ocean) and the satellite is in descending pass (see Table I), i.e., the swell is propagating toward the SAR along the range direction. The cross spectrum indicates that the energy in the swell is higher than the wind sea, which is consistent with the buoy measurements and model data.

The scatter plot illustrating the correlation is shown in Fig. 4(e) for VV (scatterplot for HH is not shown). The positive correlation between the NRCS and the Doppler variations indicates that the maxima of the NRCS and Dc occur at the same (or close) position over the long wave. It can be observed

from the scatterplot that the NRCS and Doppler variations are highly correlated. The correlation coefficient is ∼0.8 and ∼0.72 for VV and HH polarizations, respectively. The slightly lower correlation at HH polarization is mainly due to the lower SNR, and hence, larger NRCS and phase noise.

Fig. 4(f) depicts the magnitude of the cross spectrum (also called coherence) and its phase, averaged over the azimuth direction. The solid lines indicate the peaks of the coherence and the dashed lines depict the wavenumber corresponding to the observed swell (average of the ocean model and wave buoy). It is readily noticed that the coherence peaks at or very close to the swell wavenumber, which indicates high coherence. It can also be noticed that the phase shift between the NRCS and Dc is very small within ±5° at the coherence peak, which explains the high linear correlation.

2) Case Study 2 (English Channel): Fig. 5 depicts the 2-D variation of the NRCS [see Fig. 5(a)] and the Dc [see Fig. 5(b)] observed over a wave field in the English Channel area (see Fig. 2) on 13 September 2014. The sea is mixed with a wind sea propagating to the area from 60°(buoy) and 82.9°(model) and a swell propagating from 260°(model). The mixed-sea can be observed in the Dc image and the cross spectrum [see Fig. 5(c) and (d)]. It can be noticed that the energy in south-west to north-east propagating swell is larger (dominant), which is consistent with the model data in Table III, which indicates that swell amplitude is larger than wind wave amplitude (shts > shww).

Despite the broad scatterplot [see Fig. 5(e)] compared to the previous case, which is probably due the off-range propagation, a positive correlation can be identified. The swell is propagating from the Atlantic Ocean toward the English Channel and the satellite is in descending pass (see Table I), i.e., the swell is propagating toward the SAR with some angle relative to the SAR range direction, hence the positive correlation indicating that positive NRCS modulations coincide with positive orbital velocities. The correlation coefficient (r=0.65) is slightly lower than the previous case. This is probably due to the lower RAR MTF, which decreases with azimuth angle, i.e., maximum in the range direction and minimum in the flight direction. Finally, Fig. 5(f) shows that the coherence peaks (solid lines) are very close to the observed swell wavenumber (dashed lines). The phase at the peaks of about ±20°, which is larger than the previous (range traveling) case, explains the slightly lower linear correlation due to off-range propagation.

3) Case Study 3 (San Francisco Bay): Fig. 6 depicts the NRCS and Dc variations of a wave filed observed in San Francisco bay (see Fig. 2) on 12 October 2015. The bright spot in the image is likely a ship that produces a high backscatter and high Doppler shift. The sea consists of a wind sea propagating from 291°and a swell from 273°with the swell having larger amplitude, according to the model. The buoy indicates a mean wave direction from 254°. The swell field is propagating from west (pacific ocean) heading (and refracting) toward the US west coast and the satellite is in the ascending pass (see Fig. 1), i.e., the swell is moving away from the SAR with a small angle relative to the SAR range direction, hence the negative correlation as can be seen in the scatterplot presented in Fig. 6(c). According to the model data (see Table III), mdts=273° and the wave buoy

VMDR=254°, the swell is propagating with an angle 2°(model) and 32°(buoy) relative to the range direction. The latter is more consistent with the SAR image. The magnitude of the correlation coefficient (r=0.67) is lower than case 1 and comparable to case 2. This is probably due to the RAR MTF, which decreases as the angle between wave propagation and the range direction increases. The coherence [see Fig. 6(d)] peaks very close to the wavenumber of the swell observed by the ocean model and wave buoy. The phase shift at the peaks of about ±25° is larger than the case 1 and comparable to case 2, which explains the lower linear correlation.

4) Case Study 4 (Moray Firth): Fig. 7 depicts the NRCS and Dc variations observed by SAR in the Moray Firth area (see Fig. 2) on 4 January 2016. The sea consists of a wind sea coming from 107°and a swell coming from 86°, according to the model. The buoy indicate a peak wave direction VPED=93°. In this case, the amplitude of the wind wave is much larger than the amplitude of the swell, i.e., wind-sea dominant.

The wave field is propagating from the east (from North Sea) heading for the Scottish east coast and the satellite is in the descending pass, i.e., waves propagate in the range direction away from the SAR, hence the negative correlation as is illustrated in the scatter plot in Fig. 7(e). This is consistent with the cross spectrum [see Fig. 7(c) and (d)] in direction. Note, however, that the imaginary part agrees on the swell direction but disagrees on wind sea direction, with the buoy and model data.

The NRCS modulation is much stronger than cases 2 and 3, because the SWH is higher and the direction of propagation is more favorable. According to model data (see Table III) and the wave buoy, the swell is propagating with an angle 8° (model) and 15° (buoy) relative to the range direction. Both are consistent with the SAR images. The magnitude of the correlation coefficient (r=0.72) is higher than cases 2 and 3 due to the more favorable propagation direction. The coherence depicted in Fig. 7(d) shows that the NRCS and Dc variations are highly correlated at the wavenumber corresponding to the observed swell (dashed line). The phase is small within ±10°, similar to the first case, which explains the high linear correlation. It seems like the more off-range is the wave propagation direction, the larger is the phase difference and the lower is the correlation.

5) Case Study 5 (Santa Maria): Fig. 8 depicts the 2-D zero-mean NRCS and Dc variations in (a) and (b), respectively. These images were acquired over the California's coast on 14 September 2014 nearby Santa Maria. The shown part is a portion of the southern part of the original TanDEM-X scene. The images are shown only for VV polarization, as NRCS and Dc variations for HH polarization images look very similar. Both images show a clear north–south wavy pattern.

According to the model, the sea consists of a swell coming from 182°and a wind sea coming from 307°. The two buoys indicate a mean wave direction varying between 234° (southern buoy) and 295° (northern buoy). The amplitude of the wind sea (about 1 m) is larger than the amplitude of the swell (0.49 m). The swell of 143-m wavelength is traveling from south toward north Pacific ocean and the satellite is in descending pass (see Table I), i.e., the swell is propagating toward the SAR along the flight direction.
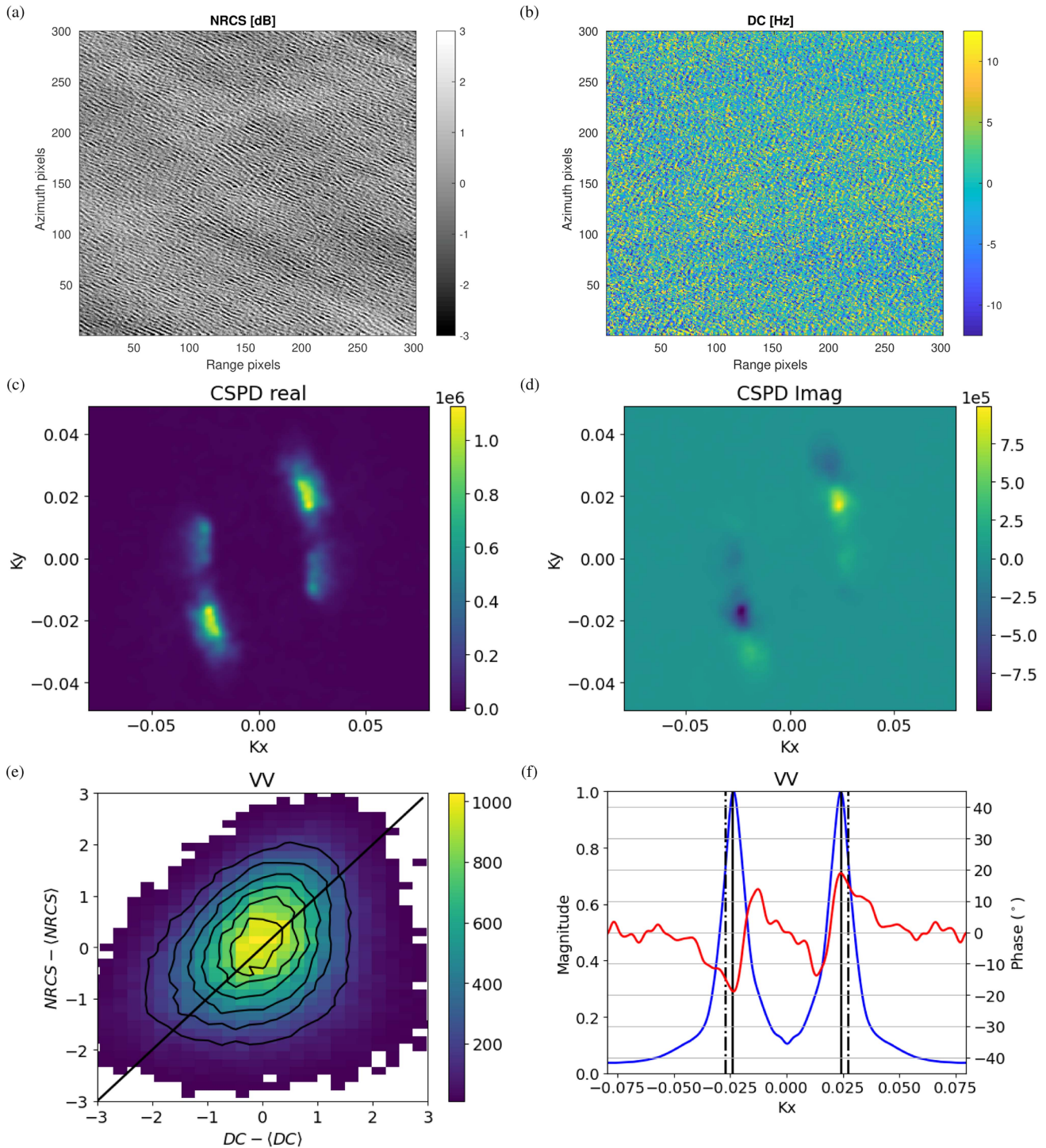
Fig. 5. English Channel—20140913—Descending pass. (a) NRCS variation. (b) Dc variation. (c) Real part. (d) Imaginary part of the cross spectrum. (e) Scatter plot of NRCS variation against Dc variation for VV, colorbar is the number of points. (f) Cross-spectrum magnitude (blue) and phase (red) for VV, averaged over azimuth direction, K_x is the range wavenumber. The solid and dashed lines depict the wavenumber at the cross-spectrum peak and the swell given by the ocean model and the wave buoy averaged.

Fig. 8(c) and (d) shows the real and imaginary parts of the cross spectrum, which agree qualitatively well with the propagation direction of the swell given by the model and the buoys. The phase shift at maximum coherence [see Fig. 8(f)] between the NRCS and the Dc is relatively large, approximately 45–50°, which explains the low linear correlation coefficient (∼0.2) [see

Fig. 8(e)]. The NRCS-weighted average of the Dc is also very small ∼0.2 Hz.

6) Case Study 6 (Pentland Firth): Fig. 9 depicts the 2-D zero-mean NRCS and Dc variations in (a) and (b), respectively. These images were acquired over the Pentland Firth on 7 June 2020. The shown image is a portion of the northwest part of
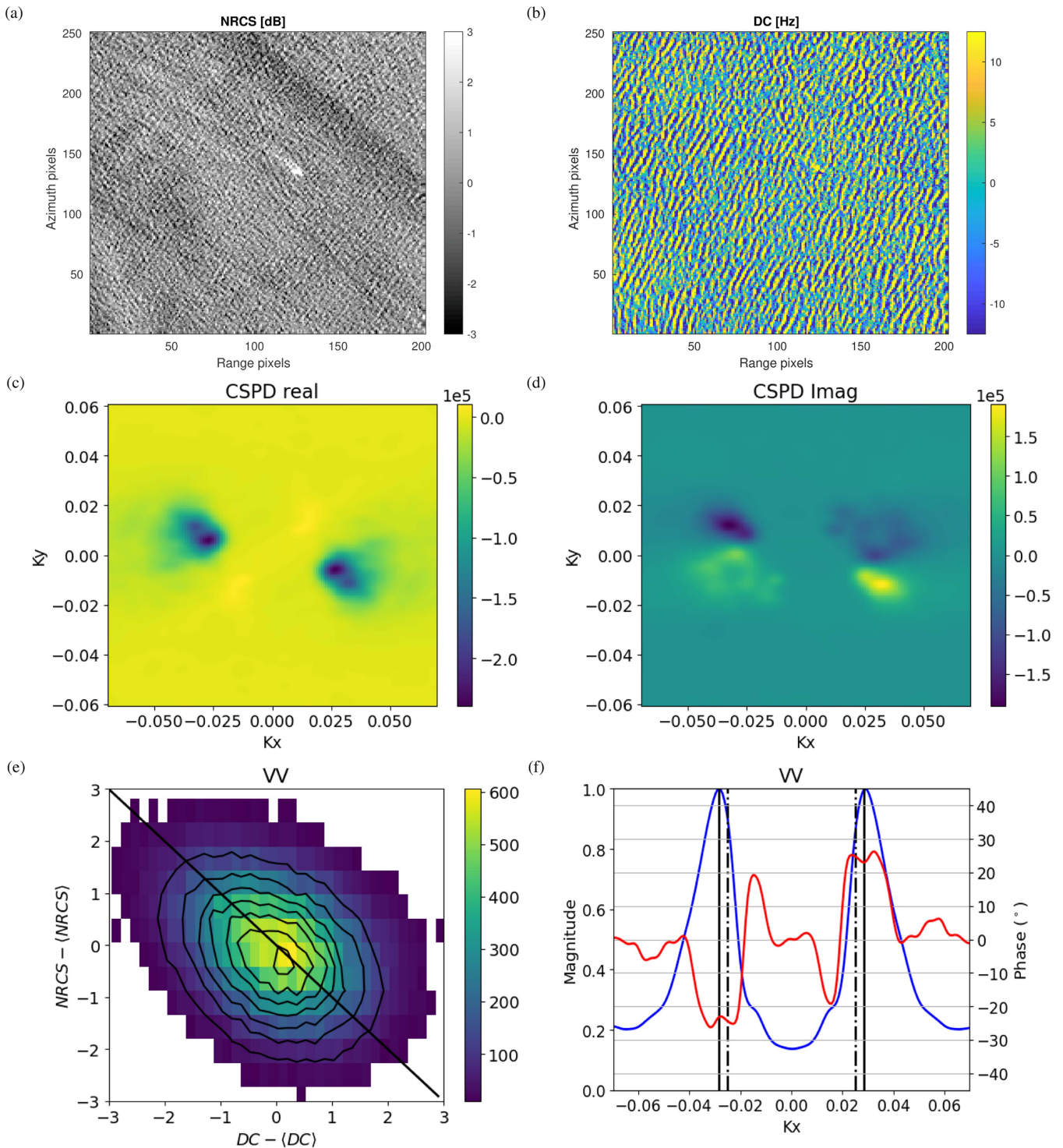
Fig. 6. San Francisco bay—20151012—Descending pass. (a) NRCS variation. (b) Dc variation. (c) Real part. (d) Imaginary part of the cross spectrum. (e) Scatter plot of NRCS variation against Dc variation. The colorbar shows the number of points per bin, bins with less than ten point not shown for clarity. (f) Cross-spectrum magnitude (blue) and phase (red), averaged over azimuth direction, K_x is the range wavenumber. The dashed lines depict the wavenumber of the swell given by the ocean model and the wave buoy averaged.

the original TanDEM-X scene. No wave buoy was found in the area, thus we rely on the model data for the interpretation. According to the model, a wind sea is coming from 348° and a swell from 346°. The swell amplitude is larger than the wind sea, i.e., swell dominant sea. The swell of 2.14-m height and 142 m is traveling from north Atlantic ocean southwards to the

north coast of Scotland and the satellite is in ascending pass (see Table I), i.e., the swell is propagating toward the SAR along the flight direction.

The cross spectrum depicted in Fig. 9(c) and (d) agrees qualitatively with the propagation direction. Note that the imaginary part indicates a south–north propagation, which disagrees with
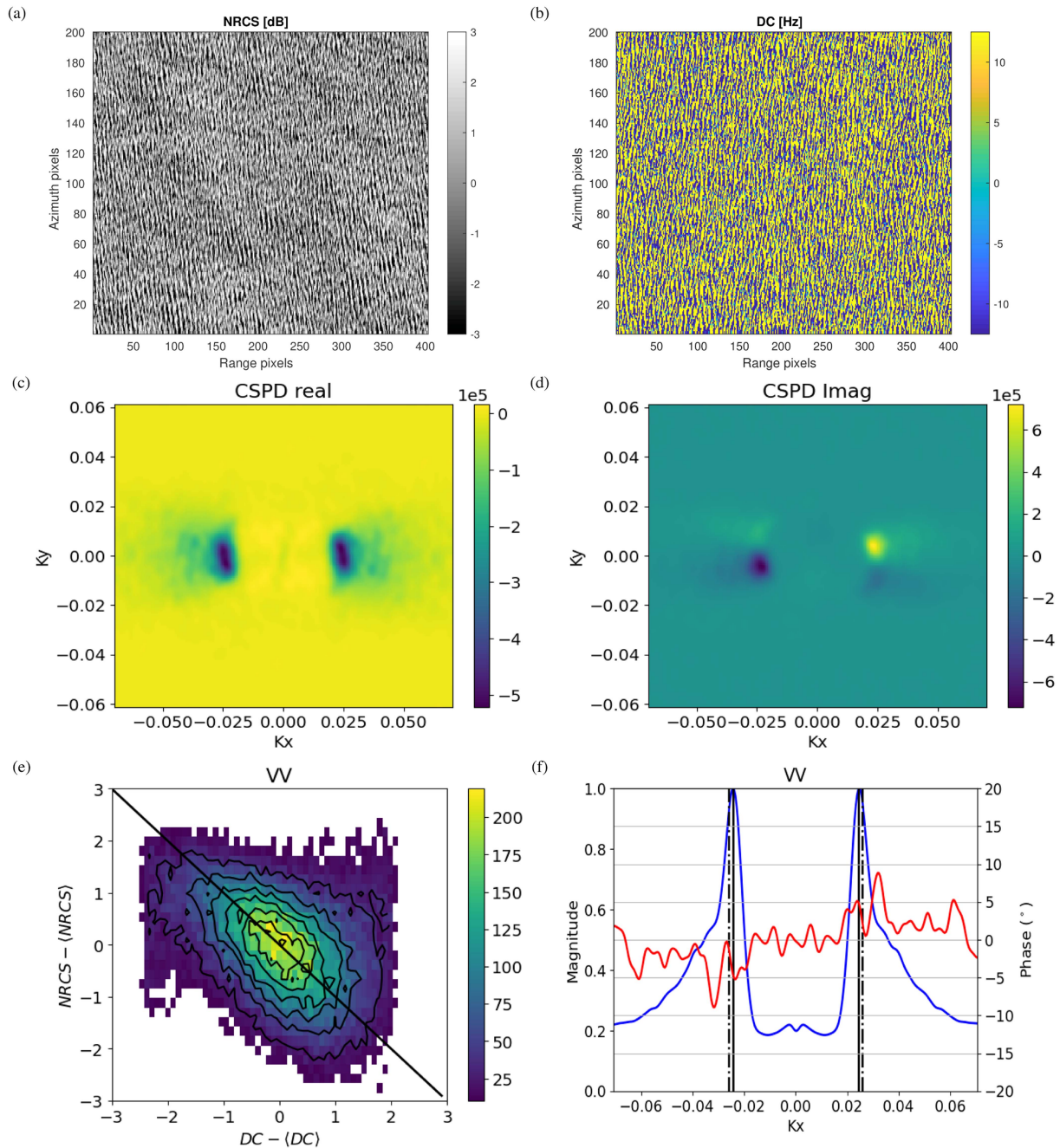
Fig. 7. Moray Firth—20160104—Descending pass. (a) NRCS variation. (b) Dc variation. The images are detrended in range and azimuth. (c) Real part. (d) Imaginary part of the cross spectrum. (e) Scatter plot of NRCS variation against Dc variation. The colorbar shows the number of points per bin, bins with less than ten point not shown for clarity. (f) Cross-spectrum magnitude (blue) and phase (red), averaged over azimuth direction, K_x is the range wavenumber. The solid and dashed lines depict the wavenumber at the cross-spectrum peak and the swell given by the ocean model and the wave buoy averaged.

model data. This is due to the fact that the NRCS-Dc cross spectrum is sensitive to the wave propagation relative to the SAR flight direction and not to the absolute direction. The phase shift depicted in Fig. 9(f) between the NRCS and the Dc is large ($\sim 60°$), consequently the linear correlation coefficient is negligible (<0.1). This can also be observed from the scatterplot [see Fig. 9(e)], which indicate the absence of linear correlation. The NRCS-weighted average of the Dc is also negligible <0.1 Hz. The latter two cases suggest that the azimuth traveling waves

contribution to the wave-induced Dc is very small due the lack of correlation.

V. Discussion

Table IV summarizes the results for the six case studies and reports the correlation coefficients, standard deviation of the NRCS and Dc, the NRCS-weighted average Dc, and the corresponding relevant acquisition and wave parameters. It can be
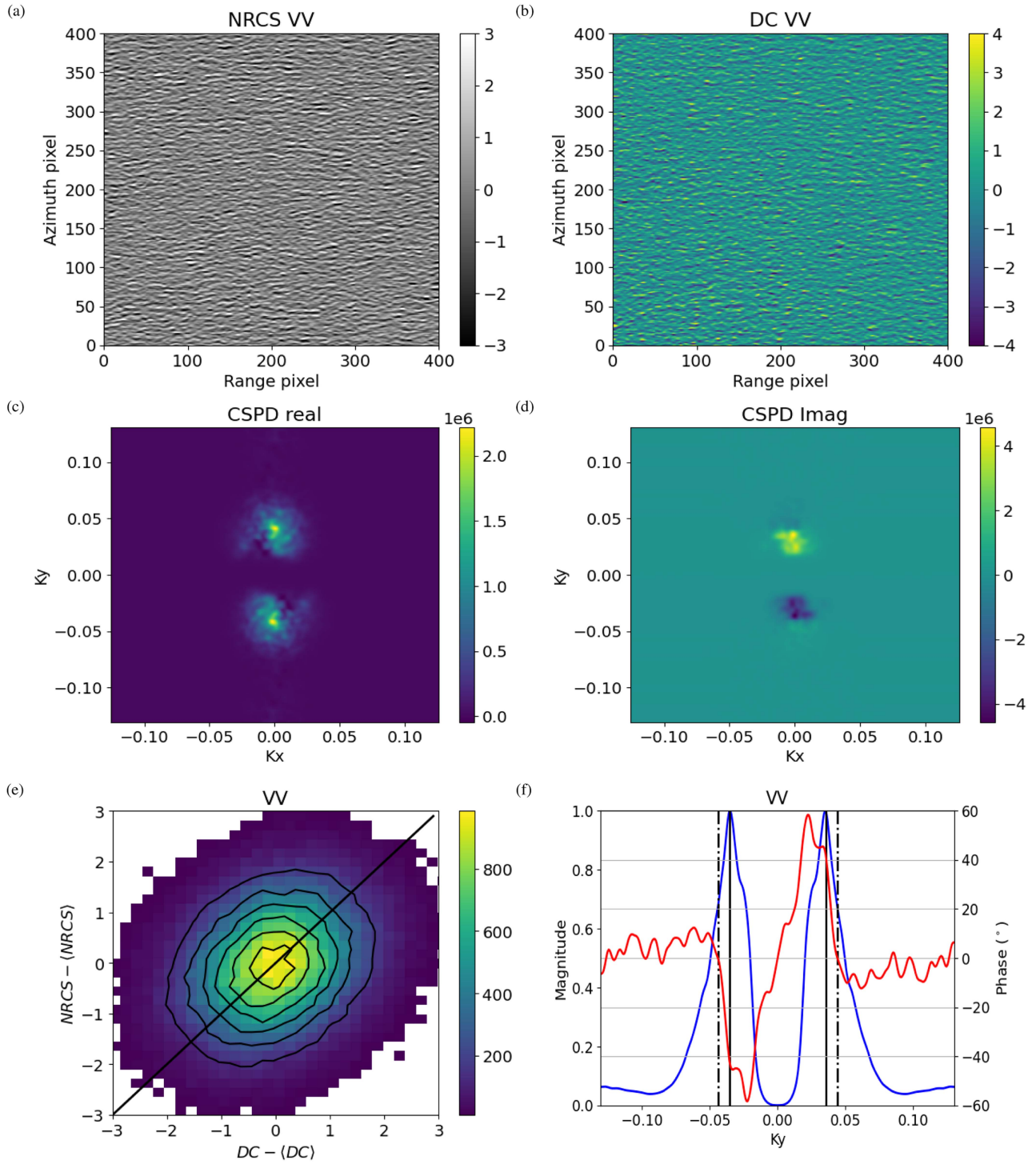
Fig. 8. Santa Maria—20140914—Descending pass. (a) NRCS variation. (b) Dc variation. The images are detrended in range and azimuth. (c) Real part. (d) Imaginary part of the cross spectrum. (e) Scatter plot of NRCS variation against Dc variation. The colorbar shows the number of points per bin, bins with less than ten point not shown for clarity. (f) Cross-spectrum magnitude (blue) and phase (red), averaged over azimuth direction, K_y is the azimuth wavenumber. The solid and dashed lines depict the wavenumber at the cross-spectrum peak and the swell given by the ocean model and the wave buoy averaged.

readily observed that the standard deviations of the Dc $\sqrt{\langle f_{\mathrm{Dc}}'^2 \rangle}$ and NRCS ($\sqrt{\langle \sigma_{\mathrm{VV}}'^2 \rangle}$) increase with the wave steepness. This is expected from the theory since the standard deviation of the Dc is proportional to the standard deviation of the wave's radial orbital velocity (σ_{or}) $\sigma_{\mathrm{Dc}} = k_e \sigma_{or}/\pi$, and σ_{or} is proportional

to ωa. Similarly, the variation of the NRCS (see Appendix) is proportional (assuming linear MTF) to the ka, i.e., the product of the wavenumber and amplitude.

The linear correlation coefficient is high for the range traveling waves and degrades as the wave propagation direction deviates
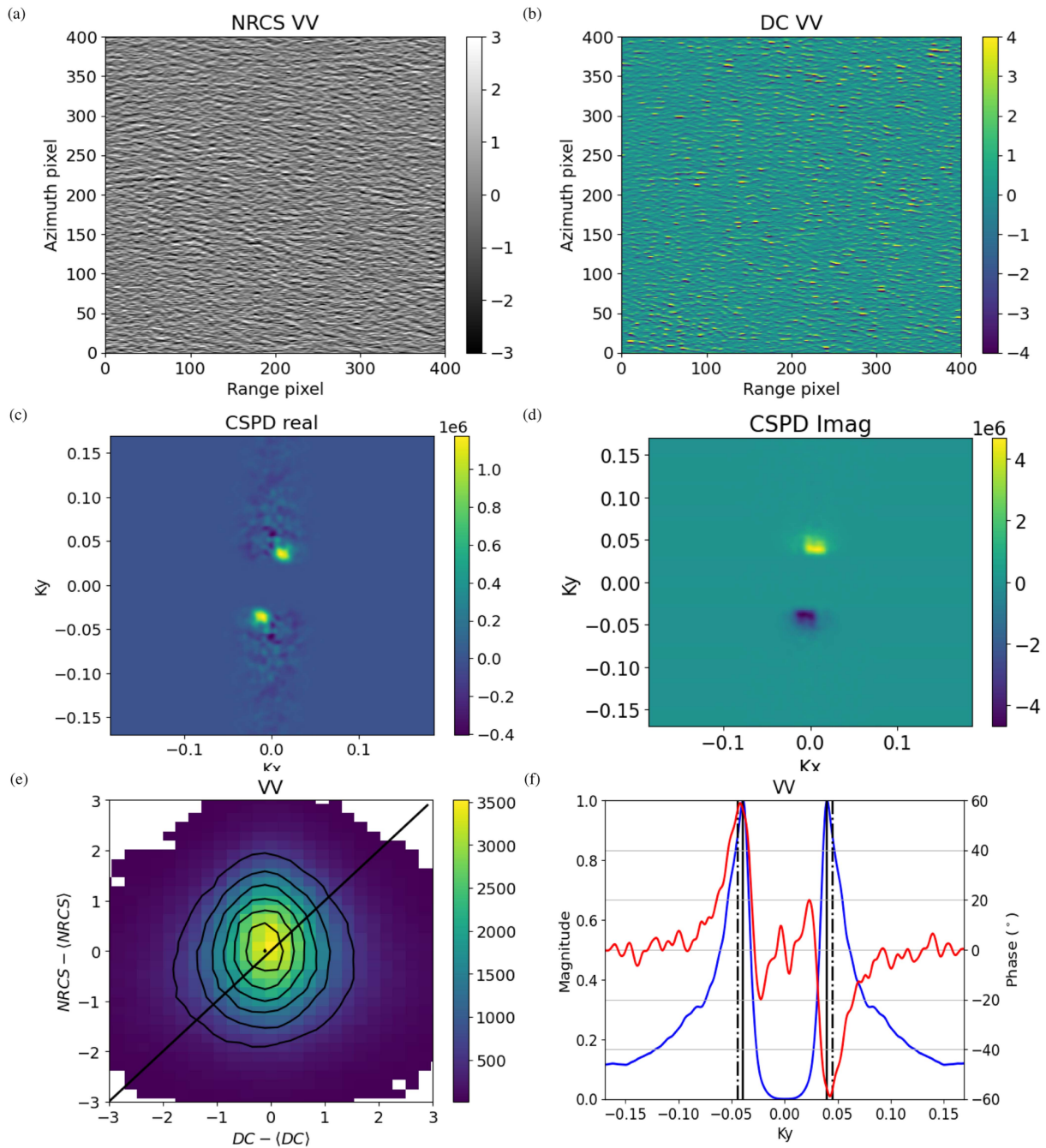
Fig. 9. Pentland Firth—20200607—Ascending pass. (a) NRCS variation. (b) Dc variation. The images are detrended in range and azimuth. (c) Real part. (d) Imaginary part of the cross spectrum. (e) Scatter plot of NRCS variation against Dc variation. The colorbar shows the number of points per bin, bins with less than ten point not shown for clarity. (f) Cross-spectrum magnitude (blue) and phase (red), averaged over azimuth direction, K_y is the azimuth wavenumber. The solid and dashed lines depict the wavenumber at the cross-spectrum peak and the swell given by the ocean model and the wave buoy averaged.

from the SAR range direction until it becomes negligible for azimuth traveling waves. Consequently, the NRCS-weighted average $\langle \sigma' \cdot f'_{Dc} \rangle$ is large for near-range traveling waves and increases in magnitude with wave steepness, and is very small to negligible for azimuth traveling waves. This is due to the fact that both NRCS and Dc modulations are proportional to wave steepness. Note that the horizontal wave-induced Doppler velocity may reach up to ∼1 m/s, which is in the order of many strong currents. The sign of the correlation coefficient and the NRCS-weighted Dc indicates the propagation direction of the swell. It is positive when the swell propagates toward the SAR and negative otherwise. The correlation coefficient and the NRCS-weighted Dc for azimuth traveling waves are generally negligible.

The cross-spectrum analysis demonstrates further that the NRCS and the Dc variations are highly coherent at the

TABLE IV
SUMMARY OF THE RESULTS AND RELEVANT WAVE PARAMETERS FROM THE MODEL AND/OR WAVE BUOYS

	Iroise Sea 2014-09-02	English Channel 2014-09-13	S. Francisco Bay 2015-10-12	Moray Firth 2016-01-04	Santa Maria 2014-09-14	Pentland Firth 2020-06-07
Satellite heading [°]	190.5	190.6	349.5	192.2	191.2	348.1
Direction (from) [°]	292.1	260.3	272.9	86.2	182	346.2
Wave length [m]	272.2	222.8	279.3	208.1	143	117
Wave height [m]	2.3	1.49	2.27	4.82	0.43	2.14
Wave steepness [×100]	0.845	0.669	0.813	2.31	0.301	1.829
Correlation coefficient	0.82	0.65	-0.67	-0.72	0.2	0.027
$\sqrt{\langle \sigma_{VV}'^2 \rangle}$ [dB]	0.77	1.27	1.13	1.96	0.18	0.29
$\sqrt{\langle f_{Dc}'^2 \rangle}$ [Hz]	10.04	5.97	10.64	51.52	0.67	8.0
$\langle \sigma' \cdot f_{Dc}' \rangle$ [Hz]	6.95	2.27	-4.17	-31.93	0.24	0.027
Radial velocity [m/s]	0.10	0.035	-0.065	-0.49	0.0037	0.0004
Horizontal velocity [m/s]	0.12	0.061	-0.12	-0.96	0.01	0.0007

The standard deviations ($\langle f_{Dc}'^2 \rangle$), ($\langle \sigma_{VV}'^2 \rangle$) and the NRCS-weighted average ($\langle \sigma' \cdot f_{Dc}' \rangle$) are calculated over the portion of the image presented in the result section for each case. The ($\langle \sigma' \cdot f_{Dc}' \rangle$) is converted to radial velocity and horizontal velocity using eq. (2).

wavenumber of the observed dominant wave. The small phase shift in the range-traveling cases explains why most of the points in the scatter plots presented previously lie close the one-to-one line. Note, that this is a special case. In general, depending on the phase shift, the NRCS-Dc relation can vary from a line (0°), ellipse (45°) to a circle (90°). For the azimuth-traveling cases, the large phase shift explains the low linear correlation.

It is worth noting that in contrast to the traditional NRCS cross spectrum, the NRCS-Dc cross spectrum is not a reliable indicator of the sense of the wave propagation direction. The imaginary part depends on the phase of the SAR MTF, which indicates whether the NRCS modulation leads or lags the Dc modulation.

To our knowledge, the only study we can compare our results to, was reported in [24]. In that study, similar correlation between the variation of the Doppler velocity and the NRCS was observed in the time domain by a fixed Ka-band scatterometer [24, Fig. 5]. However, the study does not provide quantitative evaluation of the correlation and its dependence on wave parameters. Our results agree qualitatively with [24], although here the analysis is done in the spatial (SAR image) domain. Furthermore, we simulated the swell Dc using the semiempirical model (also called KaDOP) in [20]. This model should predict the wave-induced Dc (in velocity units), which is equivalent to radial velocity in Table IV. In this simulation, the β_{ws} (see [20, eq. (16)] is set to zero, to get only the swell contribution. The obtained results with the default β_{sw} (=0.0625) are: 0.049, 0.0112, 0.069, 0.133, -0.0008, and -0.0065 m/s, for the six cases. To achieve values comparable to ours, 0.158, 0.036, 0.073, 0.425, -0.003, -0.006 m/s, the β_{sw} (see [20, eq. (16)]) to 0.2. We do not expect the model to give the same result obtained here because the model is based on a real aperture radar operating at Ka-band. Nevertheless, the predicted values are surprisingly and encouragingly close (although slightly lower) than our values and suggest that the Dc increases with wave steepness for the range-traveling waves and is one to two orders of magnitude smaller for azimuth-traveling waves.

VI. CONCLUSION

Six pairs of high resolution images of NRCS and Doppler shift acquired by the ATI-SAR system TanDEM-X over different regions have been analyzed. It is shown that, for near-range traveling waves, the NRCS and Doppler modulations are highly correlated at both polarizations VV and HH, which is due to the small phase shift between the two modulations. In addition, the sign of the correlation coefficient depends on swell propagation direction. That is, swell propagating up-range gives positive correlation, while swell propagating in down-range direction gives negative correlation. This correlation is the origin of the wave-induced velocity bias.

It is also found that the NRCS-weighted average of the Doppler shift is nonzero as expected from SAR imaging theory and increases with wave steepness. The sign of the NRCS-weighted average Dc follows the wave propagation direction. This effect was illustrated by calculating the NRCS-weighted average Dc over a portion of the SAR image. This yields values up to 0.96 m/s. This velocity bias is comparable or even often larger than the current speed to be retrieved, hence the importance of understanding and modeling the wave-induced Dc. Retrieving the current from SAR without taking into account this wave-induced Dc would result in a significant velocity bias.

For azimuth traveling waves, the linear correlation between the NRCS and the Dc is generally very low due to the large phase difference. Consequently, the NRCS-weighted Dc average, and thus, the wave-induced velocity bias is much smaller than for range-traveling waves and can often be neglected.

These unique high-resolution measurements of NRCS and Doppler shift can be used to empirically estimate the radar MTF, following time-domain studies such as [24] and [33], which is essential in wave inversion from SAR images. These data will potentially advance modeling the wave-induced Doppler, which is crucial for current retrieval from SAR. Note however, that this requires a large number of colocated NRCS/Dc images covering a variety of acquisition parameters (incidence and azimuth angles) and wave parameters (height, direction, etc.). Finally, it

is also possible to directly retrieve the wave height from images exhibiting phase-resolved waves such as those presented here. This is left for future work.

APPENDIX A
SAR MTF

The variation of the NRCS due to a long monochromatic wave assuming a linear MTF can be written as [30]

$$\sigma(x) = \sigma\left[1 + |M|a\cos(kx - \omega t + \delta)\right] \tag{11}$$

where a is the wave amplitude, and k and ω are the wave vector and radian frequency of the long wave, respectively. $|M|$ is the magnitude of the total MTF and δ is its phase.

The total RAR MTF is the sum of three MTFs representing three different mechanisms, assumed independent

$$M = M^t + M^h + M^{rb} \tag{12}$$

where M^t, M^{rb}, and M^h are the tilt, range bunching, and hydrodynamic MTFs, respectively.

The tilt M^t, range bunching M^r, and hydrodynamic M^h MTFs read [30], [31]

$$M^t = -\frac{4ik_y\cot\theta}{1 + \sin^2\theta} \tag{13}$$

$$M^r = -ik_y\cot\theta \tag{14}$$

$$M^h = -4.5\omega\frac{k_y^2}{k}\frac{\omega - i\mu}{\omega^2 + \mu^2} \tag{15}$$

$$M^v = -\frac{R}{V}\omega\frac{k_x}{k}\left(\cos\theta - i\frac{k_y}{k}\sin\theta\right) \tag{16}$$

where k_x and k_y are the ocean wave wavenumbers in the azimuth and range directions, respectively, k is the magnitude of the wavenumber, and ω is the wave radian frequency. μ is the hydrodynamic relaxation rate, set here to 0.5. R is the slant range from the SAR antenna to the target, and V is the satellite velocity.

The radial component of the wave orbital velocity is calculated as

$$V_r = (V_x\cos\phi_w + V_y\sin\phi_w)\sin(\theta) - V_z\cos\theta \tag{17}$$

where V_x, V_y, and V_z are the three components of the wave orbital velocity. ϕ_w is the relative wave propagation direction, $\phi_w = 0$ for range traveling wave. Note that C_{LW} in (2) can be expressed as $V_r = C_{\text{LW}}\sin\theta$ and f'_D in (4) is related to V_r by $f'_D = -k_e V_r/\pi$.

APPENDIX B
VELOCITY BUNCHING MODEL

According to the velocity bunching model, assuming a Gaussian antenna pattern the SAR image intensity is $I(x,y)$ is given by [30], [34]

$$I(x_i, y_i) = \iint \delta(y_i - y)\sigma(x,y)(\rho_{aN}(x,y))^{-1}$$

$$\exp - \left[\pi^2\frac{(x_i - x - (R/V)V_r(x,y))^2}{\rho_{aN}(x,y)^2}\right]dxdy$$

where (x_i, y_i) and (x, y) are the Cartesian coordinates in the image and the ocean surface, respectively. ρ_a is the single-look azimuth resolution and ρ_{aN} is the N-look azimuth resolution. $\sigma(x, y)$ is the NRCS. Here, x is in azimuth and y in the range direction.

REFERENCES

[1] D. R. Thompson, *Calculation of Microwave Doppler Spectra From the Ocean Surface With a Time-Dependent Composite Model*. Berlin, Germany: Springer, May 1989, pp. 27–40.

[2] D. R. Thompson and J. R. Jensen, "Synthetic aperture radar interferometry applied to ship generated internal waves in the 1989 loch linnhe experiment," *J. Geophysical Res., Oceans*, vol. 98, no. C6, pp. 10259–10269, 1993. [Online]. Available: https://agupubs.onlinelibrary.wiley.com/doi/abs/10.1029/93JC00429

[3] R. Romeiser and D. R. Thompson, "Numerical study on the along-track interferometric radar imaging mechanism of oceanic surface currents," *IEEE Trans. Geosci. Remote Sens.*, vol. 38, no. 1, pp. 446–458, Jan. 2000.

[4] R. Romeiser et al., *Direct Surface Current Field Imaging From Space by Along-Track InSAR and Conventional SAR*. Berlin, Germany: Springer, Feb. 2010, pp. 73–91.

[5] R. Goldstein and H. Zebker, "Interferometric radar measurement of ocean surface currents," *Nature*, vol. 328, pp. 707–709, 1987.

[6] R. Romeiser, H. Runge, S. Suchandt, R. Kahle, C. Rossi, and P. S. Bell, "Quality assessment of surface current fields from TerraSAR-X and TanDEM-X along-track interferometry and Doppler centroid analysis," *IEEE Trans. Geosci. Remote Sens.*, vol. 52, no. 5, pp. 2759–2772, May 2014.

[7] A. Elyouncha, L. E. B. Eriksson, R. Romeiser, and L. M. H. Ulander, "Measurements of sea surface currents in the Baltic sea region using spaceborne along-track InSAR," *IEEE Trans. Geosci. Remote Sens.*, vol. 57, no. 11, pp. 8584–8599, Nov. 2019.

[8] B. Chapron, F. Collard, and F. Ardhuin, "Direct measurements of ocean surface velocity from space: Interpretation and validation," *J. Geophysical Res.*, vol. 110, Mar. 2005, Art. no. C07008.

[9] J. A. Johannessen et al., "Direct ocean surface velocity measurements from space: Improved quantitative interpretation of Envisat ASAR observations," *Geophysical Res. Lett.*, vol. 35, no. 22, 2008, Art. no. L22608.

[10] M. W. Hansen, F. Collard, K. F. Dagestad, J. A. Johannessen, P. Fabry, and B. Chapron, "Retrieval of sea surface range velocities from Envisat ASAR Doppler centroid measurements," *IEEE Trans. Geosci. Remote Sens.*, vol. 49, no. 10, pp. 3582–3592, Oct. 2011.

[11] M. W. Hansen, J. A. Johannessen, K. F. Dagestad, F. Collard, and B. Chapron, "Monitoring the surface inflow of Atlantic water to the Norwegian sea using Envisat ASAR," *J. Geophysical Res. Oceans*, vol. 116, no. C12, 2011, Art. no. C12008. [Online]. Available: https://agupubs.onlinelibrary.wiley.com/doi/abs/10.1029/2011JC007375

[12] A. Elyouncha, L. E. B. Eriksson, H. Johnsen, and L. M. H. Ulander, "Using Sentinel-1 ocean data for mapping sea surface currents along the southern Norwegian coast," in *Proc. IEEE Int. Geosci. Remote Sens. Symp.*, 2019, pp. 8058–8061.

[13] A. Moiseev, J. A. Johannessen, and H. Johnsen, "Towards retrieving reliable ocean surface currents in the coastal zone from the Sentinel-1 Doppler shift observations," *J. Geophysical Res. Oceans*, vol. 127, no. 5, 2022, Art. no. e2021JC018201. [Online]. Available: https://agupubs.onlinelibrary.wiley.com/doi/abs/10.1029/2021JC018201

[14] S. Fan, B. Zhang, V. Kudryavtsev, and W. Perrie, "Mapping radial ocean surface currents in the outer core of Hurricane Maria from synthetic aperture radar Doppler measurements," *IEEE J. Sel. Topics Appl. Earth Observ. Remote Sens.*, vol. 17, pp. 2090–2097, Dec. 19, 2023.

[15] A. C. H. Martin, C. Gommenginger, J. Marquez, S. Doody, V. Navarro, and C. Buck, "Wind-wave-induced velocity in ATI-SAR ocean surface currents: First experimental evidence from an airborne campaign," *J. Geophysical Res. Oceans*, vol. 121, no. 3, pp. 1640–1653, 2016.

[16] A. Moiseev, H. Johnsen, J. A. Johannessen, F. Collard, and G. Guitton, "On removal of sea state contribution to Sentinel-1 Doppler shift for retrieving reliable ocean surface current," *J. Geophysical Res. Oceans*, vol. 125, no. 9, 2020, Art. no. e2020JC016288.

[17] A. Elyouncha, L. E. B. Eriksson, R. Romeiser, and L. M. H. Ulander, "Empirical relationship between the Doppler centroid derived from X-band spaceborne InSAR data and wind vectors," *IEEE Trans. Geosci. Remote Sens.*, vol. 60, Mar. 26, 2021, Art. no. 4201120.

[18] E. Rodríguez et al., "Estimating ocean vector winds and currents using a Ka-band pencil-beam Doppler scatterometer," *Remote Sens.*, vol. 10, no. 4, 2018, Art. no. 576. [Online]. Available: https://www.mdpi.com/2072-4292/10/4/576

[19] A. Mouche et al., "On the use of Doppler shift for sea surface wind retrieval from SAR," *IEEE Trans. Geosci. Remote Sens.*, vol. 50, no. 7, pp. 2901–2909, Jul. 2012.

[20] Y. Yurovsky, V. Kudryavtsev, S. Grodsky, and B. Chapron, "Sea surface KA-band Doppler measurements: Analysis and model development," *Remote Sens.*, vol. 11, no. 7, Apr. 2019, Art. no. 839. [Online]. Available: http://dx.doi.org/10.3390/rs11070839

[21] V. Kudryavtsev, S. Fan, B. Zhang, B. Chapron, J. A. Johannessen, and A. Moiseev, "On the use of dual co-polarized radar data to derive a sea surface Doppler model–Part 1: Approach," *IEEE Trans. Geosci. Remote Sens.*, vol. 61, Jan. 10, 2023, Art. no. 4201013.

[22] S. Fan, B. Zhang, A. Moiseev, V. Kudryavtsev, J. A. Johannessen, and B. Chapron, "On the use of dual co-polarized radar data to derive a sea surface Doppler model–Part 2: Simulation and validation," *IEEE Trans. Geosci. Remote Sens.*, vol. 61, Feb. 22, 2023, Art. no. 4202009.

[23] R. Romeiser et al., "Current measurements by SAR along-track interferometry from a space shuttle," *IEEE Trans. Geosci. Remote Sens.*, vol. 43, no. 10, pp. 2315–2324, Oct. 2005.

[24] Y. Y. Yurovsky, V. N. Kudryavtsev, B. Chapron, and S. A. Grodsky, "Modulation of Ka-band Doppler radar signals backscattered from the sea surface," *IEEE Trans. Geosci. Remote Sens.*, vol. 56, no. 5, pp. 2931–2948, May 2018.

[25] M. Hansen et al., "Simulation of radar backscatter and Doppler shifts of wave current interaction in the presence of strong tidal current," *Remote Sens. Environ.*, vol. 120, pp. 113–122, 2012.

[26] R. Bamler and P. Hartl, "Synthetic aperture radar interferometry," *Inverse Problems*, vol. 14, no. 4, 1998, Art. no. R1. [Online]. Available: http://stacks.iop.org/0266-5611/14/i=4/a=001

[27] R. F. Hanssen, *Radar Interferometry: Data Interpretation and Error Analysis*, 1st ed. Berlin, Germany: Springer, 2001.

[28] C. Werner, U. Wegmüller, T. Strozzi, and A. Wiesmann, "Gamma SAR and interferometric processing software," in *Proc. ERS–ENVISAT Symp.*, Gothenburg, Sweden, Oct. 2000, Art. no. 1620.

[29] S. N. Madsen, "Estimating the Doppler centroid of SAR data," *IEEE Trans. Aerosp. Electron. Syst.*, vol. 25, no. 2, pp. 134–140, Mar. 1989.

[30] W. Alpers, D. B. Ross, and C. L. Rufenach, "On the detectability of ocean surface waves by real and synthetic aperture radar," *J. Geophysical Res. Oceans*, vol. 86, no. C7, pp. 6481–6498, 1981. [Online]. Available: https://agupubs.onlinelibrary.wiley.com/doi/abs/10.1029/JC086iC07p06481

[31] K. Hasselmann and S. Hasselmann, "On the nonlinear mapping of an ocean wave spectrum into a synthetic aperture radar image spectrum and its inversion," *J. Geophysical Res. Oceans*, vol. 96, no. C6, pp. 10713–10729, 1991. [Online]. Available: https://agupubs.onlinelibrary.wiley.com/doi/abs/10.1029/91JC00302

[32] M. Zink et al., "TanDEM-X: 10 years of formation flying bistatic SAR interferometry," *IEEE J. Sel. Topics Appl. Earth Observ. Remote Sens.*, vol. 14, pp. 3546–3565, Feb. 26, 2021.

[33] A. Schmidt, V. Wismann, R. Romeiser, and W. Alpers, "Simultaneous measurements of the ocean wave—radar modulation transfer function at L, C, and X bands from the research platform Nordsee," *J. Geophysical Res. Oceans*, vol. 100, no. C5, pp. 8815–8827, 1995.

[34] W. A. Claus Brüning and K. Hasselmann, "Monte-Carlo simulation studies of the nonlinear imaging of a two dimensional surface wave field by a synthetic aperture radar," *Int. J. Remote Sens.*, vol. 11, no. 10, pp. 1695–1727, 1990. [Online]. Available: https://doi.org/10.1080/01431169008955125

Anis Elyouncha (Member, IEEE) received the M.S. degree in electrical engineering and telecommunications from the Universite Libre de Bruxelles, Brussels, Belgium, in 2006, and the Ph.D. degree in radio and space sciences from the Chalmers University of Technology, Gothenburg, Sweden, in 2020.

From 2008 to 2015, he was a Research Engineer with the Royal Military Academy of Belgium. From 2015 to 2023, he was a Postdoctoral Researcher with the Department of Space Earth and Environment, Chalmers University of Technology. He is currently a Researcher with the Department of Marine Sciences, University of Gothenburg, Gothenburg. His research interests include electromagnetic scattering from the ocean surface, sea surface wind, waves and currents retrieval from radar data, and air–sea interaction.

Roland Romeiser (Senior Member, IEEE) received the Diplom degree in physics from the University of Bremen, Bremen, Germany, in 1990, and the Dr.rer.nat. degree in geosciences and Habilitation degree in oceanography from the University of Hamburg, Hamburg, Germany, in 1993 and 2007, respectively.

From 1990 to 2008, he was with the Institute of Oceanography, University of Hamburg. From 1998 to 1999, he was with the Applied Physics Laboratory, Johns Hopkins University, Laurel, MD, USA, as a Feodor Lynen Fellow of the Alexander von Humboldt Foundation. In 2008, he joined the Rosenstiel School of Marine and Atmospheric Science, University of Miami, Coral Gables, FL, USA, where he is currently a full Professor. He has wide experience in the field of remote sensing of ocean currents, waves, and winds by airborne and spaceborne microwave radars. His current research interests include advanced synthetic aperture radar processing and algorithm development for current and wave retrievals.

Dr. Romeiser was an Associate Editor for the IEEE JOURNAL OF OCEANIC ENGINEERING from 2000 to 2020 and of IEEE TRANSACTIONS ON GEOSCIENCE AND REMOTE SENSING from 2014 to 2017.